RAA 2019 Vol. **19** No. **11**, 162(14pp) doi: 10.1088/1674–4527/19/11/162

http://www.raa-journal.org *http://iopscience.iop.org/raa*

***R**esearch in*
***A**stronomy and*
***A**strophysics*

The Lyman-alpha Solar Telescope (LST) for the ASO-S mission – III. data and potential diagnostics

Li Feng[1], Hui Li[1], Bo Chen[2], Ying Li[1], Roberto Susino[3], Yu Huang[1], Lei Lu[1], Bei-Li Ying[1,4], Jing-Wei Li[1], Jian-Chao Xue[1,4], Yu-Tong Yang[1,4], Jie Hong[5], Jian-Ping Li[1], Jie Zhao[1], Wei-Qun Gan[1] and Yan Zhang[6]

[1] Key Laboratory of Dark Matter and Space Astronomy, Purple Mountain Observatory, Chinese Academy of Sciences, Nanjing 210033, China; *lfeng@pmo.ac.cn*
[2] Changchun Institute of Optics, Fine Mechanics and Physics, Chinese Academy of Sciences, Changchun 130033, China
[3] INAF-Turin Astrophysical Observatory, via Osservatorio 20, 10025 Pino Torinese, Italy
[4] School of Astronomy and Space Science, University of Science and Technology of China, Hefei 230026, China
[5] School of Astronomy and Space Science, Nanjing University, Nanjing 210023, China
[6] Department of Computer Science and Technology, Nanjing University, Nanjing 210023, China

Received 2019 June 28; accepted 2019 July 23

Abstract The Lyman-alpha Solar Telescope (LST) is one of the three payloads onboard the Advanced Space-based Solar Observatory (ASO-S) mission. It aims at imaging the Sun from the disk center up to $2.5\,R_\odot$ targeting solar eruptions, particularly coronal mass ejections (CMEs), solar flares, prominences/filaments and related phenomena, as well as the fast and slow solar wind. The most prominent speciality of LST is the simultaneous observation of the solar atmosphere in both Lyα and white light (WL) with high temporospatial resolution both on the solar disk and the inner corona. New observations in the Lyα line together with traditional WL observations will provide us with many new insights into solar eruptions and solar wind. LST consists of a Solar Corona Imager (SCI) with a field of view (FOV) of 1.1 – $2.5\,R_\odot$, a Solar Disk Imager (SDI) and a full-disk White-light Solar Telescope (WST) with an identical FOV up to $1.2\,R_\odot$. SCI has a dual waveband in Lyα (121.6 ± 10 nm) and in WL (700 ± 40 nm), while SDI works in the Lyα waveband of 121.6 ± 7.5 nm and WST works in the violet narrow-band continuum of 360 ± 2.0 nm. To produce high quality science data, careful ground and in-flight calibrations are required. We present our methods for different calibrations including dark field correction, flat field correction, radiometry, instrumental polarization and optical geometry. Based on the data calibration, definitions of the data levels and processing procedures for the defined levels from raw data are described. Plasma physical diagnostics offer key ingredients to understand ejecta and plasma flows in the inner corona, as well as different features on the solar disk including flares, filaments, etc. Therefore, we are making efforts to develop various tools to detect the different features observed by LST, and then to derive their physical parameters, for example, the electron density and temperature of CMEs, the outflow velocity of the solar wind, and the hydrogen density and mass flows of prominences. Coordinated observations and data analyses with the coronagraphs onboard Solar Orbiter, PROBA-3, and Aditya are also briefly discussed.

Key words: Sun: coronal mass ejections (CMEs) — Sun: flares — Sun: solar wind — techniques: calibration

1 INTRODUCTION

The Advanced Space-based Solar Observatory (ASO-S) mission (Gan et al. 2015, 2019) aims at exploring two of the most spectacular eruptions on the Sun: solar flares and coronal mass ejections (CMEs), and their associated magnetism. The energies of solar flares and CMEs are believed to originate from the solar magnetic field. Therefore, simultaneous observation of the magnetic field, flares and CMEs, and their corresponding studies are of particular importance. To fulfill this major scientific objective, the Chinese solar physics community proposed the ASO-S

mission. It has three elaborately designed payloads: the Full-disk vector MagnetoGraph (FMG), the Lyman-alpha (Lyα) Solar Telescope (LST) (Li 2016; Li et al. 2019) and the Hard X-ray Imager (HXI), which are dedicated to observing the vector photospheric magnetic field, CMEs and flares, respectively. LST actually consists of three instruments: a Solar Corona Imager (SCI), Solar Disk Imager (SDI) and White-light Solar Telescope (WST). Among them, SCI is a coronagraph simultaneously and independently observing the inner corona in both the Lyα (121.6 ± 10 nm) and white light (WL) (700 ± 40 nm) wavebands, and has a field of view (FOV) of 1.1 to 2.5 $R_\odot$. For convenience of description, we use SCI_UV and SCI_WL to indicate the coronagraph in these two wavebands. SDI and WST focus more on the solar disk with an FOV of up to 1.2 $R_\odot$, and with wavebands in Lyα (121.6 ± 7.5 nm) and in WL (360.0 ± 2.0 nm), respectively.

The H I Lyα line is the strongest line among the ultraviolet (UV) chromospheric emission lines, and its emission in the corona is primarily contributed by two components (Gabriel 1971; Withbroe et al. 1982; Noci et al. 1987). One component is produced through the resonant scattering of chromospheric Lyα photons by the small fraction of residual neutral hydrogen in the corona; the other component is produced by the excitation of residual neutral hydrogen by collisions with free electrons. Up to now, observation of Lyα emission in regions of the solar disk has only been performed by very few instruments, e.g., the Very-high-resolution Advanced ULtraviolet Telescope (VAULT) (Korendyke et al. 2001; Vourlidas et al. 2010), the Chromospheric Lyman-Alpha Spectro-Polarimeter (CLASP) (Kano et al. 2012), the Solar Ultraviolet Measurements of Emitted Radiation (SUMER) (Wilhelm et al. 1995), and the Multi Spectral Solar Telescope Array (MSSTA) (Walker et al. 1993). Emission in the inner corona has probably only been observed by the UltraViolet Coronagraph Spectrometer (UVCS) (Kohl et al. 1995). All these instruments have revealed great science on solar structures from the disk to the inner corona. In 2020, ESA will launch the Solar Orbiter mission, onboard which the dual-waveband coronagraph Metis in Lyα and WL will observe the extended corona with an FOV ranging from 1.6 to 2.9 deg (Antonucci et al. 2012). LST onboard ASO-S will, for the first time, seamlessly image the full Sun with SDI and the inner corona with SCI up to 2.5 $R_\odot$, offering an excellent opportunity to reveal and track the structures in Lyα from their formation to their early evolution. To use the Lyα resonantly scattered component for plasma diagnostics, incident chromospheric emission is crucial for computing emergent emission in the corona. Equipped with both SDI and SCI_UV, LST provides a favorable functionality for such diagnostics. Besides observations in Lyα, LST also hosts a WL coronagraph (SCI_WL) which can perform linear polarization measurements (Feng et al. 2019) and a full-disk telescope in WL, aiming at studying WL flares.

As ASO-S has a Sun-synchronous orbit with an altitude of about 720 km, we do not have severe telemetry limitations. Therefore, LST is able to acquire data in the Lyα and WL channels independently and simultaneously with high cadence and spatial resolution. It is beneficial to address all the major scientific objectives of LST which are mostly dedicated to solar eruptions. To be more specific, we aim at improving our understanding of the initiation and early evolution of CMEs; the eruption of optically thick to thin prominence plasma; heating and acceleration processes in solar flares; the relationship between CMEs, eruptive prominences and solar flares; the acceleration of solar energetic particles; and the structure, energy deposition and acceleration of the solar wind. The science goals addressed with LST observations will also profit from synergy with the other two payloads, FMG and HXI, onboard ASO-S. FMG observes the photospheric magnetic field from which we can extrapolate the coronal magnetic field to derive the magnetic context of eruptions, and to study the role of the magnetic field in channeling the solar wind. HXI reveals non-thermal properties of solar flares which are complementary to the flare characteristics discovered by LST. On the other hand, coordinated observations obtained by simultaneous space-based and ground-based instruments dedicated to solar physics and heliophysics will also shed light on the major scientific objectives of LST.

The science data pipeline produces data products at different levels. As soon as science telemetry is received, the pipeline combines telemetry packets from different data products including science data, ancillary spacecraft and instrument engineering data, decompresses and reorganizes them according to time, and writes the level 0 uncalibrated data products as flexible image transport system (FITS) files. The calibration data are prepared in a similar way. As a second step, by using different types of calibration data the pipeline processes the level 0 data into level 1 data. It includes the calibration of dark current, flat field and stray light suppression (only for SCI-WL), and indexing of bad, missing and cosmic ray pixels. The result is saved in level 1 FITS files. A further step of the data processing produces level 2 data in a procedure which radiometrically calibrates the data products to physical units, converts the onboard time to Coordinated Universal Time (UTC), and converts the instrument coordinate system to

Table 1 Key Parameters of the LST Instrument Performance

Parameter	SCI_WL	SCI_UV	SDI	WST
Diameter	60 cm		60 mm	130 mm
Waveband	700.0 ± 40.0 nm	121.6 ± 10.0 nm	121.6 ± 7.5 nm	360.0 ± 2.0 nm
FOV	$1.1 - 2.5\,R_\odot$		$0.0 - 1.2\,R_\odot$	$0.0 - 1.2\,R_\odot$
Spatial resolution	$\sim 4.8''$		$\sim 1.2''$	$\sim 1.2''$
Image size	2048×2048		4608×4608	4608×4608
Cadence (routine)	60 s[a]	30 s	40 s	120 s
Cadence (event)	30 s[a]	15 s	4 s or 10 s[b]	1 – 2 s or 5 s[b]
Cadence (user)	user-defined	user-defined	user-defined	user-defined

[a] The downlink cadence for a set of polarization measurements at three polarizer positions;
[b] The former is the downlink cadence for a subregion image of 1024×1024 centered at a flare, and the latter is the cadence for a full-size image.

the World Coordinate System (WCS). We have a plan to distribute level 1 and level 2 data to the scientific community. Higher-level data are derived with our various diagnostic tools, for instance, CME mass, electron density, electron temperature, etc.

This paper is organized as follows: Section 2 is an overview of LST scientific objectives, instrument design and observing modes. Section 3 introduces our definition of the different levels of data products and the processing procedures. In Section 4, we describe our data calibration processes which include the calibration of dark currents, flat fields and radiometry. For SCI_WL, extra calibration of instrumental polarization and stray light suppression is required as well. Section 5 is dedicated to the potential physical diagnostics we are developing and will develop for CMEs, flares, prominences, solar wind, etc. The last section presents our conclusions.

2 OVERVIEW OF LST SCIENTIFIC OBJECTIVES, INSTRUMENT DESIGN AND OBSERVING MODES

2.1 Overview of the Scientific and Operational Objectives

LST is mostly devoted to observations of solar eruptions; its major scientific objectives are more concentrated in the physics related to CMEs, flares and prominences/filaments. However, as LST has the capability to observe the solar wind, we are looking into the corresponding science as well. A detailed description of the scientific objectives can be found in Li et al. (2019) in this special issue. Here we only list the major scientific objectives:

- initiation and early evolution of CMEs;
- eruption of optically thick to thin prominence/filament plasma;
- heating and acceleration processes in solar flares;
- the relationship between CMEs, eruptive prominences/filaments and solar flares;
- formation of shock waves and acceleration of solar energetic particles;
- structure, energy deposition and acceleration of fast and slow solar wind.

Besides the scientific objectives, LST also has an operational objective which is to provide data and technical support for the prediction of solar eruptions. More specifically, we have set a priority of downlinking the CME data obtained by LST, and will distribute those data to different space weather prediction centers in China within two hours once the Science Operation and Data Center (SODC) of ASO-S receives the data. After data downlink and archiving, different automatic detection, tracking and cataloging procedures are planned for CMEs, flares and prominences/filaments observed by LST. On the other hand, based on the LST data, different prediction centers should activate their prediction systems to make solar eruption predictions.

2.2 Overview of LST Instruments

LST consists of three instruments: SCI, SDI and WST. We refer readers to Chen et al. (2019) in this special issue for more details on the instrumentation of LST. Here we only summarize the major characteristics of LST. The key parameters of the LST instrument's performance are listed in Table 1. Among the three telescopes incorporated in LST, SCI is a dual-waveband coronagraph simultaneously and independently observing the inner corona in both Lyα (121.6 ± 10 nm, SCI_UV) and WL (700 ± 40 nm, SCI_WL) and has an FOV of 1.1 to $2.5\,R_\odot$. A beam splitter is installed. One path of light is transmitted to the WL channel and goes through a Stokes polarimeter. The other path is reflected to the Lyα channel and passes through the corresponding filter. SDI and WST focus more on the solar disk with FOVs up to $1.2\,R_\odot$, and with wavebands in Lyα (121.6 ± 7.5 nm) and in WL (360.0 ± 2.0 nm), respectively. We use complementary metal oxide semiconductor (CMOS) detectors made by the Changchun Institute of

Optics, Fine Mechanics and Physics (CIOMP) in China for all these three instruments. There is also a guide telescope installed on LST to increase precision of the pointing and stability of the imaging system. It observes the solar disk up to $1.2\,R_\odot$ in the waveband of 570.0 ± 5.0 with four photodiodes as the detector. It has a primary mirror with a 30 mm diameter and a time cadence of 300 Hz.

2.3 Overview of LST Observing Modes

We have classified the observing modes of LST into four categories, i.e., routine mode, event mode, user mode and calibration mode. In this subsection, we briefly introduce the former three modes and leave the different calibration modes to Section 4. The switch between the routine mode and event mode is designed to be automatic, while the switch between the routine mode and user mode is manual, made by uploading an observation plan in advance. The key observation parameters for the different modes, particularly routine and event modes, are specified in Table 2 for SCI_UV, SCI_WL, SDI and WST. In routine mode, SCI_UV has alternating short and long exposure times of one minute. Therefore, the sampling and downlink cadence is the average of these two exposure times. SCI_WL produces three polarized images in three polarizer positions of –60, 0 and 60 deg. In routine mode, it takes a set of three images in 30 s. The cadence of 10 s refers to the average time for a single frame in the image set of three frames. We have designed automatic in-flight algorithms to switch between the routine and event modes. At the same time, the start time $T_{\rm start}$, end time $T_{\rm end}$ and position of the cutout region are automatically determined as well. In the event mode, due to the large variation in intensity, we have devised automatic exposure time control (AEC) to obtain optimal exposure for SCI_UV and SDI. If the cutout fails, SDI and WST take images in the full FOV. The user mode gives freedom to users for specific science and observed target. Please note that all the values in Table 2 may be preliminary; there might be slight changes in the future. For details on the observing mode, we refer readers to Li et al. (2019).

3 DATA PRODUCTS AND PROCESSING LEVELS

The definitions of data products and processing levels are presented in Table 3. In-flight telemetry from LST is received by the Science Mission Operation Center (SMOC) in the National Space Science Center (NSSC) of China to produce level 0 data, and is propagated by using a file transfer network exclusively from ASO-S to the SODC in Purple Mountain Observatory for further data processing. Q0 and level 0 are obtained directly from SMOC. After the telemetry is received by SODC from SMOC, the level 1 and 2 data of LST are expected to be ready within 24 hours routinely — more specifically, the level 1 data within 16 h and the level 2 data within the subsequent 8 h. We give priority to the data products dedicated to space weather prediction. The frames with CME structures observed by SCI_WL are released within two hours after we receive the telemetry. In the future, level 1 and level 2 data will be released and are expected to be used by scientists most frequently. The data pipeline is currently written in IDL with the possibility of some functionalities being written in Python, after the IDL version has been developed and fully tested. The data processing software is planned to be integrated into the Solar Software (SSW) package.

Based on the calibration images obtained with the method described in Section 4, data are processed from level 0 to level 1 by correcting dark current and flat fields, and indexing bad/missing/spike pixels for all three instruments. For SCI_WL, an extra step needs to be performed. We need to remove stray light as much as possible to make coronal structures prominent by creating proper background images, e.g., monthly minimum images. To process the data from level 1 to level 2, radiometric calibration is applied to convert Digital Number (DN) to physical units. Optionally, we will offer users the functionality to scale images to a common plate scale, translate images to a common image center, rotate solar north to image north, and fix bad/missing/spike pixels by switching on different keywords in the related procedures. Consequently, users can produce 1.5 or 2.5 data by themselves using the procedures we provide. Level 3 data are devoted to the analyzed physical quantities, although we have not consolidated the exact list of quantities. The foreseen possible science products will include polarized brightness, total brightness, CME mass and density maps, etc., derived with the diagnostic tools described in Section 5.

4 DATA CALIBRATION

To obtain science-level LST data, ground and in-flight calibrations are necessary to ensure data quality. Ground laboratory calibrations are performed in CIOMP. The launch and operating environment are harsh, and the CMOS sensors may degrade with time; thus there are benefits for post-launch calibrations as well. Similar to those of other coronagraphs and full-disk imagers in space, LST calibrations include dark current and flat field correction, radiometry, instrumental polarization and stray light suppression. Note that the calibration method is not consolidated at this

Table 2 Key Parameters of the LST Observing Modes

Mode	Observation time Start	End	Sampling Cadence (s)	Downlink Cadence (s)	Image size X	Y	Image origin X	Y
			SCI_UV					
routine	yymmdd hh:mm:ss		30	30	2048	2048	0	0
event	$T_{\rm start}$	$T_{\rm end}$	15	15	2048	2048	0	0
user	yymmdd hh:mm:ss		user-defined	user-defined	user-defined		user-defined	
			SCI_WL					
routine	yymmdd hh:mm:ss		10	20	2048	2048	0	0
event	$T_{\rm start}$	$T_{\rm end}$	10	10	2048	2048	0	0
user	yymmdd hh:mm:ss		user-defined	user-defined	user-defined		user-defined	
			SDI					
routine	yymmdd hh:mm:ss		10	40	4608	4608	0	0
event (cutout)	$T_{\rm start}$	$T_{\rm end}$	4	4	1024	1024	programmed	
event (full FOV)	$T_{\rm start}$	$T_{\rm end}$	10	10	4608	4608	0	0
user	yymmdd hh:mm:ss		user-defined	user-defined	user-defined		user-defined	
			WST					
routine	yymmdd hh:mm:ss		10	120	4608	4608	0	0
event (cutout)	$T_{\rm start}$	$T_{\rm start}$+5 min	1	1	1024	1024	programmed	
	$T_{\rm start}$+5 min	$T_{\rm start}$+10 min	2	2	1024	1024	programmed	
event (full FOV)	$T_{\rm start}$	$T_{\rm start}$+10 min	5	5	4608	4608	0	0
user	yymmdd hh:mm:ss		user-defined	user-defined	user-defined		user-defined	

Table 3 Data Products and Processing Levels

Level	Processing	Unit
level 0	decompressing and rearranging raw data, adding keywords and writing to FITS files	DN
Q_0	making quicklook images of level 0 data	
level 1	correcting dark current and flat fields, suppressing stray light, indexing bad/missing/spike pixels	DN
level 1.5	optional: scaling, translating, rotating solar north to image north fixing bad/missing/spike pixels	DN
level 2	performing radiometric calibration	MSB[a] for SCI_WL erg s^{-1} cm^{-2} sr^{-1} for the rest
level 2.5	optional: scaling, translating, rotating solar north to image north fixing bad/missing/spike pixels	MSB for SCI_WL erg s^{-1} cm^{-2} sr^{-1} for the rest
level 3	optional: producing polarized brightness, total brightness, mass, electron density, electron temperature, etc.	corresponding physical units
Q_1	optional: making quicklook images of selected data from level 1 to 3	

Notes: [a] means solar brightness.

stage and may be subject to change with the progress of the mission.

4.1 Dark Current

The objective of dark current calibration is to subtract the CMOS bias and dark current noise from an observed image. The measurement of dark current is carried out with the instrument shutter closed. As the dark current of the LST CMOS detector is closely related to exposure time and temperature, we are making a model of dark current as a function of these two quantities. The CMOS bias is acquired by using the shortest exposure time available. To reduce random noise, for a given exposure time and temperature we usually take a sequence of dark current images and use their mean as the final dark current image.

4.2 Flat Field

4.2.1 Laboratory flat field calibration

Flat-field correction is performed to remove artifacts that are caused by variations in the pixel-to-pixel sensitivity of the CMOS detector. The CMOS detector is known to have a fixed-mode pattern noise, therefore we are trying to produce proper flat fields to minimize its influence. In

the laboratory, flat field calibration in WL for SCI_WL and WST is conducted in normal laboratory conditions through uniform lightening onto the instrument system. A uniform light source is achieved by an integrating sphere. The flat field calibration in Lyα for SCI_UV and SDI is more complicated and has to be done in a vacuum tank. First we use a pinhole at the focus of an Extreme Ultraviolet (EUV) / Far Ultraviolet (FUV) collimator to produce Lyα parallel light. The incident light generated by a Vacuum Ultraviolet (VUV) deuterium lamp has to pass through the Lyα filter before going to the collimator. In the next step, we put an MgF_2 diffuser in front of the instrument and use the parallel light to illuminate it; then the diffuser can be regarded as an extended uniform target which can cover the CMOS detector. Afterwards, the instrument takes flat field images of the diffuser. To decrease random noise, a sequence of images are taken and averaged. To improve the precision of the flat field calibration, we have also applied the Kuhn-Lin-Loranz (KLL) flat fielding method (Kuhn et al. 1991; Chae 2004) which does not require a uniformly illuminated target.

4.2.2 In-flight flat field calibration

After ASO-S is launched, we plan to adopt the KLL scheme (Kuhn et al. 1991; Chae 2004) for the in-flight flat field calibration of WST, SDI and possibly SCI_UV. Concerning WST and SDI, the KLL scheme requires the pointing of the spacecraft to be offset from the Sun-spacecraft direction for a series of values. Choosing the series of offset values has to fulfill two criteria: After WST or SDI takes all offset images, the combined set of their FOVs has to cover all pixels and be larger than the nominal FOV of WST or SDI; for a given pixel of an image without offset, it has to be imaged at least twice with different offset values by the instrument for later derivation of the flat field by using a least-squares fitting method. We have devised a preliminary combination of offset values. Their final quantities will be determined during the test phase after launch. During the flat field calibration of WST and SDI, we need to prevent sunlight from entering the focal plane assembly (FPA) of SCI to protect the instrument.

Flat-field calibration for SCI is performed in a different way. We install a *steady* light emitting diode (LED) calibration lamp onboard at the light entrance window of the CMOS detector box. For SCI_WL, we choose a calibration LED light source in the WL spectral range. Its light beam passes through the WL filter and then the detector records the corresponding flat field image. However, the calibration light source for SCI_UV in Lyα has a large volume and weight, which are not suitable for in-flight calibration. Therefore, we plan to use a UV LED light source instead. The light beam illuminates the detector directly and then the corresponding flat field image is taken. Please note that a flat field obtained in such a way mostly refers to the flat field of the detector. It is not the flat field of the entire SCI instrument. To overcome this disadvantage, we will use the detector's flat field and instrument flat field obtained on the ground as references. As the detector performance, especially its degradation, is probably the most relevant factor that will affect the distribution of the flat field after launch, we will monitor the in-fight detector flat field from time to time and compare it with the ground flat fields to obtain a revised instrument flat field.

4.3 Radiometry

4.3.1 Laboratory radiometric calibration

The initial preflight radiometric calibration to obtain the conversion factor between detector values on DN and physical units is performed in the laboratory. For SCI_WL and WST, we use an integrating sphere in the WL waveband with known measured radiance at its exit port to measure the radiometric response of the instrument. Unfortunately for the Lyα line used by SCI_UV and SDI, we do not have such an integrating sphere with known radiance, and have been making much efforts to devise a radiometric calibration source by ourselves in CIOMP. Our preliminary design of the calibration source includes a VUV deuterium lamp, a Lyα filter, an MgF_2 diffuser, a small target with known size, an FUV collimator and a vacuum tank. Due to the wide range of intensity of the structures from the solar disk to the inner corona, the detectors have to respond to signals from very bright to very weak and may reach beyond the linear response regime. Therefore, we need to vary the radiance of the calibration source to obtain the range in which the detector still has a linear response.

4.3.2 In-flight radiometric calibration

For SCI and SDI, in-flight radiometric calibration is mainly carried out with a set of stars which are carefully selected using the VizieR service. Because the selected calibration stars have different brightness, in the radiometric calibration mode the exposure times are adapted to the instrument sensitivity. For SDI, the brightness of the calibration stars is much weaker than the brightness of the solar disk. Therefore, the spacecraft has to be pointed from the Sun-spacecraft direction with a maximal angle of about 30 degrees to collect a sufficient number of calibration stars. On the other hand, observations of transiting plan-

ets in the SCI FOV can also be used to establish absolute radiometric calibrations. The radiometric calibration of WST is relatively easy, because in the waveband centered at 360 nm we can use the standard tables for reference solar spectral irradiances from the American Society of Testing and Materials (ASTM) G173-03. The frequency of calibration after launch can be done at any necessary time in the normal observing mode. Note that during the calibration for the different instruments, the detector may receive extremely bright and weak signals and have a nonlinear response. Therefore, when we choose the exposure time, it has to be tuned in such a way that the detector response is still in its linear regime.

4.4 Instrumental Polarization

Calibration of instrumental polarization is performed for SCI_WL which has the capability to measure the polarized brightness of the inner solar corona from 1.1 to 2.5 $R_\odot$. Incident polarized light may change its polarization state, for example, when it is reflected by the mirrors in the instrument. Therefore, we need to measure the instrument demodulation matrix instead of using the theoretical one according to the polarimeter we implement. In the case of SCI_WL, the polarimeter is a rotating filter wheel with three linear polarizers at three different polarization angles of –60, 0 and 60 deg (Feng et al. 2019). The mathematical methods of ground and in-flight polarization calibration to derive the demodulation matrix are similar. The only difference is that in the laboratory we install a polarimetric calibration unit to produce a known polarized light incident on SCI, whereas after launch this calibration unit is replaced by some carefully selected polarimetric calibration stars. On the ground, the polarimetric calibration unit is composed of a light pipe simulating the unpolarized parallel Sun light and a linear polarizer with a motor to change its orientation angle. The output of the calibration unit is linearly polarized light with its polarization state derived according to the orientation angle set up in the calibration unit. In fact, the calibration unit is designed to produce a group of linearly polarized lights in at least three linearly-independent polarization states. This group of polarized light is then used as the input to the WL path of the coronagraph which has the capability to output the intensity of the exit light with the linear polarizer of SCI_WL at –60, 0 and 60 degrees, respectively. Through such a design of the measurements, the demodulation matrix of the instrument can be inverted. By analogy, for the in-flight polarimetric calibration, we also need at least three calibration stars with linearly-independent polarization states to mimic the polarimetric calibration unit in the laboratory. We have looked for such stars. Unfortunately, at the moment we have only found two stars which satisfy our criteria without off-pointing the spacecraft. We will keep searching among the feasible stars. If no further stars will be added, we may need to roll the spacecraft to simulate the polarimetric calibration unit on the ground.

4.5 Stray Light

Stray light is the most important issue in the design of a WL coronagraph. We measure the level of stray light suppression in the laboratory before launch. We aim to achieve $10^{-6}\,B_\odot$ at $1.1\,R_\odot$ and $5 \times 10^{-8}\,B_\odot$ at $2.5\,R_\odot$. For more details on how to suppress stray light and test the level of stray light in the SCI FOV, we refer readers to Chen et al. (2019). After launch, in-flight testing of the level of stray light is indirectly done by comparing the measured brightness of stars and/or planets in the SCI FOV with their known brightness.

5 POTENTIAL PLASMA DIAGNOSTICS

LST is designed to investigate solar eruptions. Thus, we have been developing different diagnostic tools to derive important physical parameters and analyze their processes. In particular, we are targeting CMEs, flares, prominences and filaments. However, we are not restricted to studying eruptions. As LST has the capability to diagnose solar wind, we also plan to develop diagnostic techniques to derive, for instance, the outflow speed. Some other interesting phenomena may be proposed by different users. One such example is the coronal fluctuations observed by SCI. Moreover, SDI has an excellent capability to observe the quiet-Sun chromosphere and lower transition region. Since the Lyα line samples the layer/temperature between the formation heights/temperatures of the Ca II H line observed with Hinode/SOT and C II 1335 Å observed with Interface Region Imaging Spectrograph (IRIS), it is likely that the most prominent dynamic features in the quiet chromosphere and transition region, chromospheric spicules and transition region network jets, will be observed well with SDI. These ubiquitous jets serve as bridges between the lower atmosphere and corona, and thus are important in mass and energy transport in the solar atmosphere related to the problems of coronal heating and the solar wind origin. In the future, we may enrich our diagnostic tools according to the feedback of users. Note that the diagnostic tools described below are those that are currently being developed, and are also those that are in our list of future plans.

5.1 Diagnostic Tools for CMEs

CMEs are the most important observed targets for LST. To understand their onset and early evolution, the LST team has made a lot of progress related to the study of CMEs. The light from the corona has three components: K corona, F corona and E corona. SCI_WL observes the K corona which is photons from the photosphere scattered by free electrons in the corona according to Thomson scattering (van de Hulst 1950). For the E corona in the Lyα line observed by SCI_UV, it has two major components. One is the radiative component produced by resonant scattering of choromospheric Lyα photons off coronal neutral hydrogen; the other is the collisional component generated by the electron impact excitation of neutral hydrogen (Gabriel 1971).

Based on the polarimetric measurement of SCI_WL at different polarizer orientations of –60, 0 and 60 deg, total brightness (tB), polarized brightness (pB) and some other polarimetric quantities can be derived with the demodulation matrix obtained in Section 4.4. Data analysis with the conventional WL coronagraph data has been carried out for some decades. Although this has not been finalized, based on the observations of SCI_WL, we tentatively plan to offer users IDL routines or data products of the different properties of CMEs as listed below. Some examples of the data products are illustrated in Figure 1.

- Mass and density maps: Mass is a key ingredient to understand CME dynamics and energetics (Feng et al. 2013b, 2015a,b). To produce a 2D mass map, we utilize a tB or pB coronagraph image and apply the theory of Thomson scattering. The scattering angle in the related formula of Thomson scattering can be assumed as 90 deg with the CME in the plane of the sky, or alternatively, calculated from the results of 3D reconstruction below. The upper row of Figure 1 shows one example of a mass map from the coronagraph observations recorded by Solar Terrestrial Relations Observatory (STEREO) A and B. Further density maps can be derived by assuming a proper line-of-sight (LOS) depth, e.g., using the width of the CME at that LOS as an approximation.
- Radial velocity maps: Radial velocity maps are crucial for evaluating the Doppler dimming effect in the radiative component of the Lyα line and calculating the kinetic energy distribution, as well as other quantities, within a CME (Ying et al. 2019). In the middle row of Figure 1, we present a radial velocity map derived with a cross-correlation technique applied to the three consecutive COR1 coronagraph images at t_{n-1}, t_n and t_{n+1}. The difference between three panels from left to right is that the images at t_n and t_{n+1}; t_n and t_{n-1}; and t_{n-1}, t_n and t_{n-1} are used for calculation.
- 3D reconstruction of CMEs: We have two independent methods for 3D reconstruction of CMEs. One only requires observation from a single perspective and has been successfully applied to a full-halo CME (Lu et al. 2017). This category of CMEs is the most geoeffective. The position of an electron along each LOS within a CME is calculated from the Thomson-scattering angle determined with the WL coronagraph polarimetric measurements. It improves the polarization ratio method (Moran & Davila 2004) by removing structures in coronagraph images that are irrelevant with respect to the CME, and further integrates the Graduated Cylindrical Shell (GCS) fitting method (Thernisien et al. 2009). In the future, when multi-viewpoint observations are available, e.g., with Metis onboard Solar Orbiter, the mask fitting method can be applied (Feng et al. 2012, 2013a).
- Automatic detection and tracking of CMEs with a machine learning technique: With the accumulation of data accumulating from coronagraph observations, the detection and tracking of CMEs have to be done automatically for the timely distribution of CME frames for space weather forecast, and also for automatically cataloging key CME parameters for statistical studies. Thanks to the excellent performance of machine learning in image classification, and feature detection and tracking, we have applied this technique to the coronagraph images taken by LASCO C2 and it turns out that machine learning has quite a few advantages compared with the conventional segmentation technique (Wang et al. 2019). After the launch of ASO-S, we will apply this new technique to SCI_WL images.
- When the CME speed is higher than the fast magnetosonic speed, a shock may be driven and appear in the coronagraph images as a thin layer of enhanced emission located ahead of the CME front. Analysis of the dynamics of CME-driven shocks in WL images can be used to infer the average magnetic field strength thanks to measurement of the shock geometry, velocity and plasma compression ratio which are related to the Alfvén Mach number and Alfvén velocity (Bemporad & Mancuso 2010; Susino et al. 2015). The derived shock parameters together with shock-magnetic field geometry are very useful for understanding the acceleration of solar energetic particles.

A big advantage of SCI is that we have simultaneous dual-waveband coronagraph observations in WL and

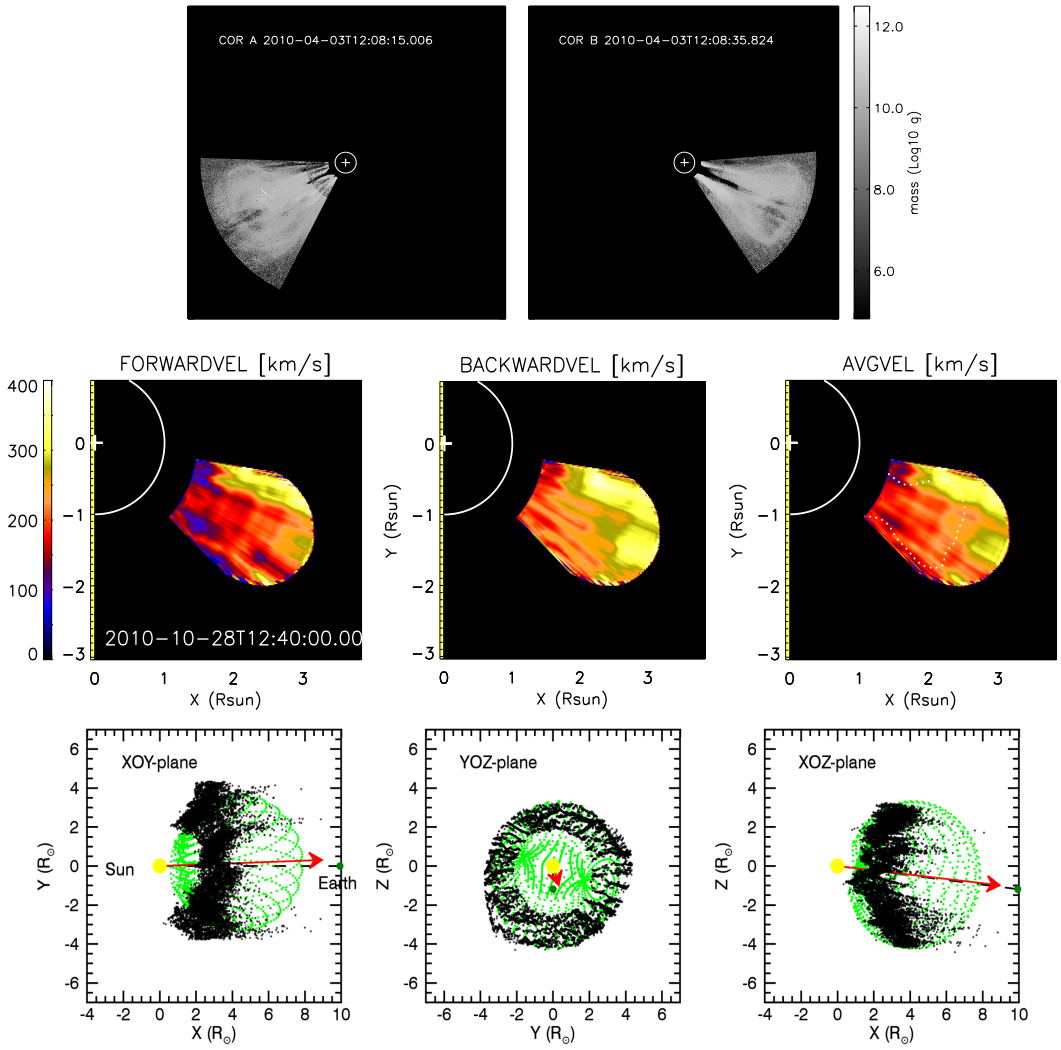

Fig. 1 *Top row*: 2D mass map of a CME calculated from STEREO coronagraph images using the theory of Thomson scattering. *Middle row*: 2D radial velocity map of a CME calculated with three consecutive COR1 coronagraph images by applying a cross-correlation technique. *Bottom row*: Reconstructed 3D CME with polarimetric method in *black* and a further GCS fitting in *green*. The three figures are adopted from Feng et al. (2015b), Ying et al. (2019) and Lu et al. (2017), respectively.

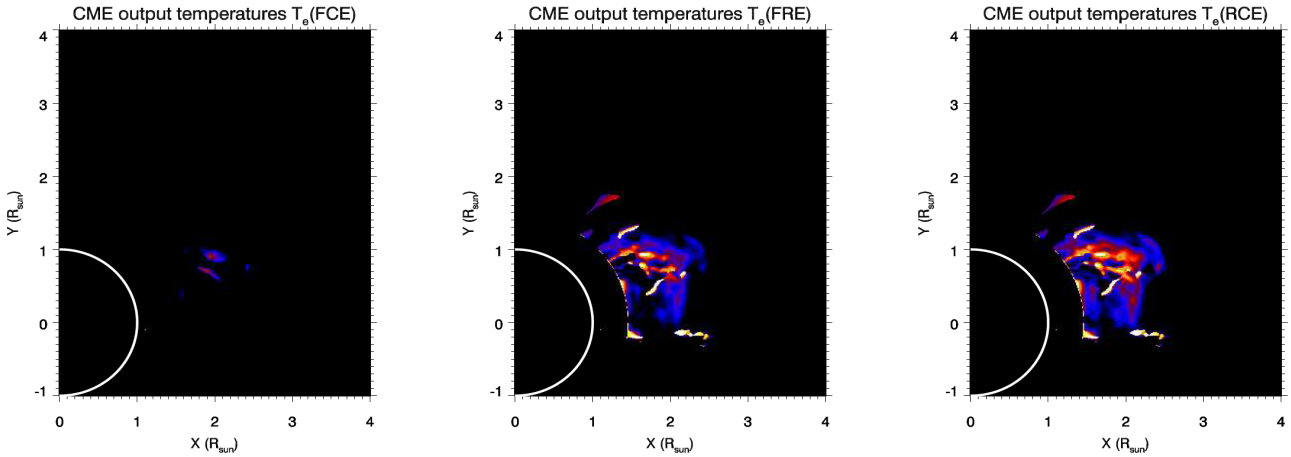

Fig. 2 *From left to right*: temperature distribution of a simulated CME derived by assuming the Lyα emission is fully collisional, fully radiative, and partially radiative and partially collisional respectively. This figure is from Bemporad et al. (2018).

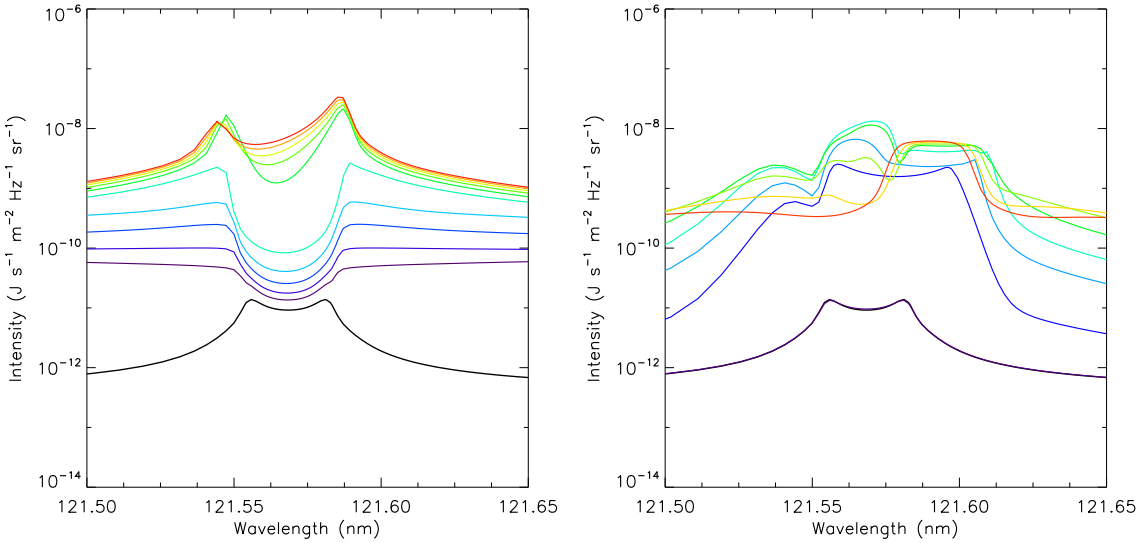

Fig. 3 Simulated evolution of the Lyα line profile at time instances of 0 to 10 s from *black* to *red* in cases of nonthermal heating (*left*) and thermal heating (*right*).

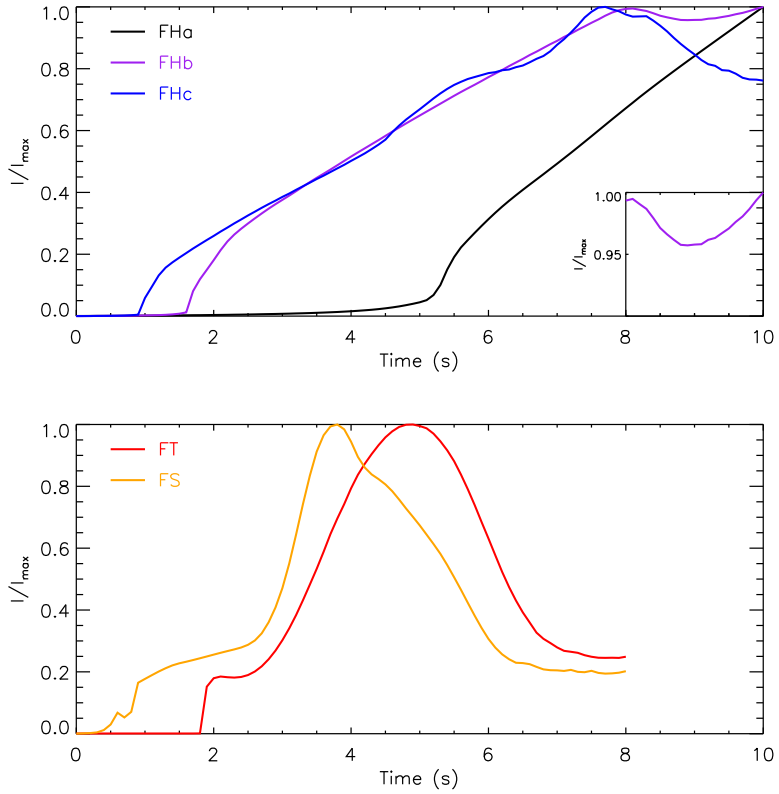

Fig. 4 Simulated light curves of integrated Lyα line intensity in cases of nonthermal heating (*top*) and thermal heating (*bottom*). This figure is from Hong et al. (2019).

Lyα. Their combination allows us to derive more information on CMEs. Most excitingly, we have Lyα observation not only in the extended corona taken by SCI_UV, but also in the solar disk taken by SDI. There are two benefits from these seamless observations from the disk to inner corona. Firstly, we can track the ejecta from their birth to their early evolution. Secondly, SDI provides valuable information on the incident chromospheric Lyα emis-

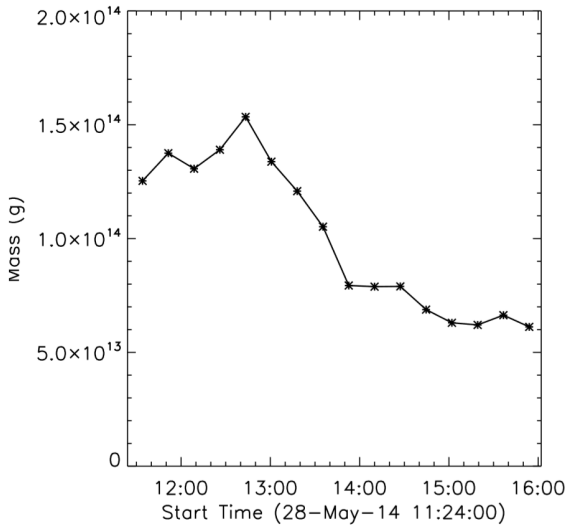

Fig. 5 The prominence mass derived from IRIS Mg II spectral observations and PROM7 non-LTE calculations. This figure is from Zhang et al. (2019).

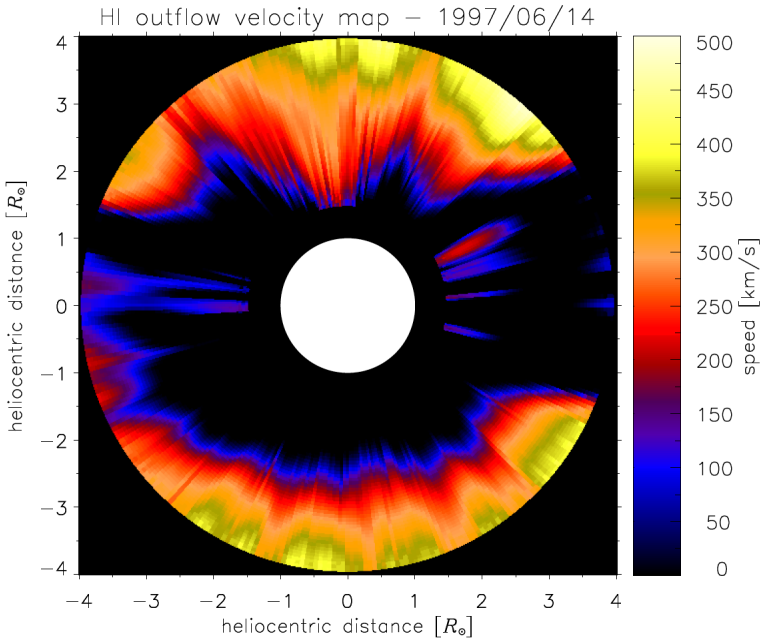

Fig. 6 The distribution of outflow velocity inferred from UVCS data acquired on 1997 June 14. This figure is adopted from Dolei et al. (2018).

sion affecting the radiative component in the corona. A Carrington map of the chromospheric emission will be created as the input for both SCI and Metis. By combining the dual-waveband observations, another important parameter, the temperature of the CME plasma, can be derived. The method has been developed and tested using magnetohydrodynamics (MHD) simulations (Bemporad et al. 2018) or real data from LASCO C2 and UVCS (Susino & Bemporad 2016). From left to right, Figure 2 presents the derived temperature distribution of a simulated CME by assuming the Lyα emission is fully collisional, fully radiative, and partially radiative and partially collisional respectively, which is adopted from Bemporad et al. (2018). The derived temperature is very valuable for the thermodynamic analysis of CMEs. In the future, the temperature obtained with observations by SCI will be compared to the temperature derived with observations by the Visible Emission Line Coronagraph (VELC, Prasad et al. 2017) onboard the Indian Aditya mission. However, we need to mention that at the moment the obtained temperatures in Bemporad et al. (2018) are overall underestimated, and cannot be applied to plasma with a high temperature of

about 10 MK and expanding radially outward faster than about 300 km s^{-1} due to very weak Lyα intensity. In the future, evaluation of the hypothesis of ionization equilibrium, equal ion and electron temperatures, isotropic thermal velocity distributions, etc., will be conducted. We will also incorporate the new radial velocity map described in Ying et al. (2019) to derive a more precise temperature map.

5.2 Diagnostic Tools for Flares

Flares are another important observing target for LST. When a flare occurs, the Lyα emission is greatly enhanced (e.g., Milligan et al. 2014), which will be observed by SDI. In addition, some flares also manifest WL continuum brightenings (i.e., white light flares, WLFs; Machado et al. 1986; Fang & Ding 1995) that can be detected by WST. The 360 nm passband is actually very important for WLF studies since it is below the Balmer limit. One type of WLF often displays a Balmer jump, which can be observed with WST. Therefore, LST allows us to study the physical processes of flares in these two promising passbands.

The emission in the Lyα passband is dominated by the Lyα line (Curdt et al. 2001) which is optically thick and formed in the middle-to-upper chromosphere and low transition region through a complex radiative transfer process. Therefore, radiative transfer modeling is needed to diagnose the physical processes that produce the Lyα emission. On the other hand, the WL continuum emission in WLFs is believed to originate from the lower chromosphere and upper photosphere (e.g., Ding 2007) and can also be calculated by radiative transfer modeling.

There are (at least) two sets of radiative transfer modeling methods that can be applied to simulate and calculate the Lyα and WL emissions as well as their temporal evolutions for flares: (1) RADYN (Carlsson & Stein 1992; Allred et al. 2015; Hong et al. 2019) plus RH (Uitenbroek 2001; Pereira & Uitenbroek 2015) in the 1D regime; and (2) MURaM (Rempel 2017; Cheung et al. 2019) plus Multi3D (Leenaarts & Carlsson 2009) in the 3D regime. Note that RADYN takes into account thermal conduction as well as nonthermal electrons, while MURaM includes thermal conduction only. Nevertheless, both are the most state-of-the-art radiative hydrodynamic simulations aimed at flares in their own regimes. These simulations can be used to diagnose the following physical processes/quantities of flares.

(1) Heating mechanism. Three primary heating mechanisms have been proposed for flares: nonthermal electron beams, thermal conduction and Alfvén waves. The former two exhibit distinguishable features in the line profile (see Fig. 3) as well as integrated line intensity (Fig. 4 of Lyα). For the latter one, there is an indication that it has different characteristics from the nonthermal beam heating mechanism (Kerr et al. 2016). The radiative hydrodynamic simulation results can be compared with future Lyα and WL imaging observations from LST to diagnose the flare heating mechanisms, especially when combined with some spectroscopic observations, e.g., those from the IRIS.

(2) Heating function. When, where and how much the plasma is heated, i.e., the flare heating function (e.g., Qiu et al. 2012), is worth investigating via multi-thread radiative transfer modeling, or a pseudo-3D RADYN. The heating function could be constrained from the Lyα and WL imaging observations from LST and validated by comparing the synthetic light curves and/or Doppler velocities with the observed ones from some other instruments (Li et al. 2012, 2014).

(3) Plasma temperature, density, velocity, etc. Once the above two issues are addressed well, radiative transfer modeling will give temporospatial variations of the plasma temperature, density, velocity, etc. (Hong et al. 2019), especially in the low atmosphere during flares. Alternatively, these quantities could be derived through statistically studying the relationship with the integrated Lyα line intensity (or WL emission) in simulations and then applying it to the LST observations.

The LST team has been simultaneously developing the above diagnostics in the 1D regime. Cases in 3D are planned to be developed in the future.

5.3 Diagnostic Tools for Prominences and Filaments

Modeling the radiative transfer processes out of Local Thermodynamic Equilibrium (LTE) is fundamental to retrieving the correct plasma parameters in erupting prominences because plasma can still be optically thick. Heinzel et al. (2016) developed a diagnostic tool based on the 1D non-LTE Multi-level Accelerated Lambda Iteration (MALI) code and determined the physical parameters of an erupting prominence embedded in the core of a CME using a combination of the UVCS Lyα line and LASCO C2 observations. This method provides the gas pressure, electron density and optical thickness of the prominence plasma, and builds a basis for future diagnostics for Metis. We plan to use it as a reference for future LST observations as well. On the other hand, Vial et al. (2019) and Zhang et al. (2019) applied another non-LTE radiative transfer code, PROM7, to investigate the relationship between integrated line intensity and plasma quantities, e.g., density and effective thickness, and derived the total hydrogen density and mass flows of an eruptive prominence (see Fig. 5).

The PROM7 code can also be employed for the non-LTE radiative transfer of filaments. In the future, prominences and filaments will be observed by SDI and SCI, Metis and also the He I D3 images taken by ASPIICS (Lamy et al. 2010) onboard PROBA-3. Combination of these observations and the non-LTE radiative transfer will provide important diagnostic results for prominences and filaments. On the other hand, Jenkins et al. (2018) adopted a simpler method to estimate the density and mass of filaments, which can be compared to the results derived with the aforementioned more complicated methods. Moreover, automated detection and tracking of prominences and filaments are also planned by adopting and modifying the methods that are currently designed for EUV images at 30.4 nm (Wang et al. 2010) and for Hα images (Hao et al. 2013).

5.4 Diagnostic Tools for Solar Wind

The solar wind originates from the continuous flow of the expanding corona. Taking advantage of the dual-waveband Lyα and WL observations of the steady solar corona, we will be able to obtain the distribution of the wind outflow velocity based on the Doppler dimming effect of the radiative component of the Lyα emission (e.g., Fig. 6, which is adopted from Dolei et al. 2018). For the radiative component of the Lyα line, the hydrogen kinetic temperature can be approximated using the results from an extended database derived by Dolei et al. (2016) from UVCS observations, while the electron density of the global corona can be obtained from the WL coronagraph images according to Thomson scattering theory. By comparing the derived outflow velocity distribution with the global magnetic field structures extrapolated from the photospheric magnetic field measurements, e.g., Tadesse et al. (2014) by another payload FMG onboard ASO-S, we will be able to infer the relationship between fast and slow solar wind streams and the magnetic field structures.

6 CONCLUSIONS

In summary, we present the data products and potential diagnostic tools for LST onboard ASO-S. After a brief overview of the scientific objectives, instrument design and observing modes, we emphasize the data products of LST in this paper. In particular, we describe our data calibration methods both on the ground and in flight to obtain level 1 and level 2 data. For higher-level LST data, much effort is being devoted to the diagnostic tools we have developed and are going to develop in the future.

Acknowledgements This work is supported by the National Natural Science Foundation of China (Grant Nos. 11522328, 11473070, 11427803 and U1731241), by the CAS Strategic Pioneer Program on Space Science (Grant Nos. XDA15010600, XDA15052200, XDA15320103 and XDA15320301), and the National Key Research and Development Program (2018YFA0404202).

References

Allred, J. C., Kowalski, A. F., & Carlsson, M. 2015, ApJ, 809, 104

Antonucci, E., Fineschi, S., Naletto, G., et al. 2012, in Society of Photo-Optical Instrumentation Engineers (SPIE) Conference Series, 8443, Space Telescopes and Instrumentation 2012: Ultraviolet to Gamma Ray, 844309

Bemporad, A., & Mancuso, S. 2010, ApJ, 720, 130

Bemporad, A., Pagano, P., & Giordano, S. 2018, A&A, 619, A25

Carlsson, M., & Stein, R. F. 1992, ApJ, 397, L59

Chae, J. 2004, Sol. Phys., 221, 1

Chen, B., Li, H., Song, K. F., et al. 2019, RAA (Research in Astronomy and Astrophysics), 19, 159

Cheung, M. C. M., Rempel, M., Chintzoglou, G., et al. 2019, Nature Astronomy, 3, 160

Curdt, W., Brekke, P., Feldman, U., et al. 2001, A&A, 375, 591

Ding, M. D. 2007, in Astronomical Society of the Pacific Conference Series, 368, The Physics of Chromospheric Plasmas, eds. P. Heinzel, I. Dorotovič, & R. J. Rutten, Heinzel

Dolei, S., Spadaro, D., & Ventura, R. 2016, A&A, 592, A137

Dolei, S., Susino, R., Sasso, C., et al. 2018, A&A, 612, A84

Fang, C., & Ding, M. D. 1995, A&AS, 110, 99

Feng, L., Inhester, B., & Gan, W. 2015a, ApJ, 805, 113

Feng, L., Inhester, B., & Mierla, M. 2013a, Sol. Phys., 282, 221

Feng, L., Inhester, B., Wei, Y., et al. 2012, ApJ, 751, 18

Feng, L., Li, H., Inhester, B., et al. 2019, RAA (Research in Astronomy and Astrophysics), 19, 059

Feng, L., Wang, Y., Shen, F., et al. 2015b, ApJ, 812, 70

Feng, L., Wiegelmann, T., Su, Y., et al. 2013b, ApJ, 765, 37

Gabriel, A. H. 1971, Sol. Phys., 21, 392

Gan, W. Q., Zhu, C., Deng, Y. Y., et al. 2019, RAA (Research in Astronomy and Astrophysics), 19, 156

Gan, W., Deng, Y., Li, H., et al. 2015, in Proc. SPIE, 9604, Solar Physics and Space Weather Instrumentation VI, 96040T

Hao, Q., Fang, C., & Chen, P. F. 2013, Sol. Phys., 286, 385

Heinzel, P., Susino, R., Jejčič, S., Bemporad, A., & Anzer, U. 2016, A&A, 589, A128

Hong, J., Li, Y., Ding, M. D., & Carlsson, M. 2019, arXiv:1905.13356

Jenkins, J. M., Long, D. M., van Driel-Gesztelyi, L., & Carlyle, J. 2018, Sol. Phys., 293, 7

Kano, R., Bando, T., Narukage, N., et al. 2012, in Society of Photo-Optical Instrumentation Engineers (SPIE) Conference Series, 8443, Space Telescopes and Instrumentation 2012:

Ultraviolet to Gamma Ray, 84434F
Kerr, G. S., Fletcher, L., Russell, A. J. B., & Allred, J. C. 2016, ApJ, 827, 101
Kohl, J. L., Esser, R., Gardner, L. D., et al. 1995, Sol. Phys., 162, 313
Korendyke, C. M., Vourlidas, A., Cook, J. W., et al. 2001, Sol. Phys., 200, 63
Kuhn, J. R., Lin, H., & Loranz, D. 1991, PASP, 103, 1097
Lamy, P., Damé, L., Vivès, S., & Zhukov, A. 2010, in Society of Photo-Optical Instrumentation Engineers (SPIE) Conference Series, 7731, Space Telescopes and Instrumentation 2010: Optical, Infrared, and Millimeter Wave, 773118
Leenaarts, J., & Carlsson, M. 2009, in Astronomical Society of the Pacific Conference Series, 415, The Second Hinode Science Meeting: Beyond Discovery-Toward Understanding, eds. B. Lites, M. Cheung, T. Magara, J. Mariska, & K. Reeves, 87
Li, H. 2016, in IAU Symposium, 320, Solar and Stellar Flares and their Effects on Planets, eds. A. G. Kosovichev, S. L. Hawley, & P. Heinzel, 436
Li, H., Chen, B., Feng, L., et al. 2019, RAA (Research in Astronomy and Astrophysics), 19, 158
Li, Y., Qiu, J., & Ding, M. D. 2012, ApJ, 758, 52
Li, Y., Qiu, J., & Ding, M. D. 2014, ApJ, 781, 120
Lu, L., Inhester, B., Feng, L., et al. 2017, ApJ, 835, 188
Machado, M. E., Avrett, E. H., Falciani, R., et al. 1986, in The Lower Atmosphere of Solar Flares, ed. D. F. Neidig & M. E. Machado, 483
Milligan, R. O., Kerr, G. S., Dennis, B. R., et al. 2014, ApJ, 793, 70
Moran, T. G., & Davila, J. M. 2004, Science, 305, 66
Noci, G., Kohl, J. L., & Withbroe, G. L. 1987, ApJ, 315, 706
Pereira, T. M. D., & Uitenbroek, H. 2015, A&A, 574, A3
Prasad, B. R., Dipankar, B., Singh, J., & Subramanya, N. 2017, Current Science, 113, 613
Qiu, J., Liu, W.-J., & Longcope, D. W. 2012, ApJ, 752, 124
Rempel, M. 2017, ApJ, 834, 10
Susino, R., & Bemporad, A. 2016, ApJ, 830, 58
Susino, R., Bemporad, A., & Mancuso, S. 2015, ApJ, 812, 119
Tadesse, T., Wiegelmann, T., Gosain, S., MacNeice, P., & Pevtsov, A. A. 2014, A&A, 562, A105
Thernisien, A., Vourlidas, A., & Howard, R. A. 2009, Sol. Phys., 256, 111
Uitenbroek, H. 2001, ApJ, 557, 389
van de Hulst, H. C. 1950, Bull. Astron. Inst. Netherlands, 11, 135
Vial, J.-C., Zhang, P., & Buchlin, É. 2019, A&A, 624, A56
Vourlidas, A., Sanchez Andrade-Nuño, B., Landi, E., et al. 2010, Sol. Phys., 261, 53
Walker, Jr., A. B. C., Timothy, J. G., Hoover, R. B., & Barbee, Jr., T. W. 1993, in Proc. SPIE, 1742, Multilayer and Grazing Incidence X-Ray/EUV Optics for Astronomy and Projection Lithography, eds. R. B. Hoover, & A. B. C. Walker, Jr., 630
Wang, P. Y., Zhang, Y., Feng, L., et al. 2019, ApJS, 244, 9
Wang, Y., Cao, H., Chen, J., et al. 2010, ApJ, 717, 973
Wilhelm, K., Curdt, W., Marsch, E., et al. 1995, Sol. Phys., 162, 189
Withbroe, G. L., Kohl, J. L., Weiser, H., & Munro, R. H. 1982, Space Sci. Rev., 33, 17
Ying, B., Bemporad, A., Giordano, S., et al. 2019, ApJ, 880, 41
Zhang, P., Buchlin, É., & Vial, J.-C. 2019, A&A, 624, A72